ACSNANO

www.acsnano.org

ARTICLE

Highly Negative Poisson's Ratio in Thermally Conductive Covalent Organic Frameworks

Ashutosh Giri,* Austin M. Evans, Muhammad Akif Rahman, Alan J. H. McGaughey, and Patrick E. Hopkins*

Cite This: *ACS Nano* 2022, 16, 2843−2851

Read Online

ACCESS | Metrics & More | Article Recommendations | Supporting Information

ABSTRACT: **The prospect of combining two-dimensional materials in vertical stacks has created a new paradigm for materials scientists and engineers. Herein, we show that stacks of two-dimensional covalent organic frameworks are endowed with a host of unique physical properties that combine low densities, high thermal conductivities, and highly negative Poisson's ratios. Our systematic atomistic simulations demonstrate that the tunable mechanical and thermal properties arise from their singular layered architecture comprising strongly bonded light atoms and periodic laminar pores. For example, the negative Poisson's ratio arises from the weak van der Waals interactions between the two-dimensional layers along with the strong covalent bonds that act as hinges along the layers, which facilitate the twisting and swiveling motion of the phenyl rings relative to the tensile plane. The mechanical and thermal properties of two-dimensional covalent organic frameworks can be tailored through structural modularities such as control over the pore size and/or interlayer separation. We reveal that these materials mark a regime of materials design that combines low densities with high thermal conductivities arising from their nanoporous yet covalently interconnected structure.**

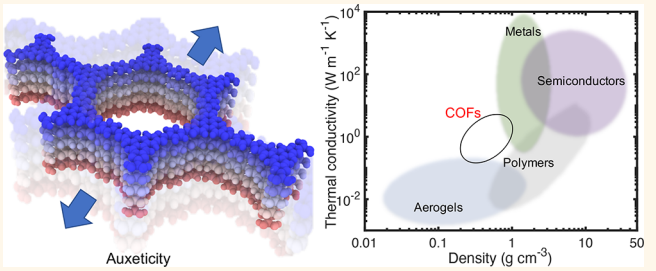

KEYWORDS: *Covalent organic frameworks, high negative Poisson's ratio, auxetic materials, anisotropic thermal conductivity, 2D polymers*

INTRODUCTION

The design of multifunctional materials that combine several advantageous physical properties for various technologically relevant applications is one of the most fundamental scientific challenges. One such emerging class of materials showing potential to drastically enhance a plethora of applications is two-dimensional (2D) covalent organic frameworks (COFs) formed by polymerizing monomers into macro-molecular sheets linked by strong covalent bonds.[1−3] With the advent of modern fabrication technologies, 2D COFs with atomically precise, permanently porous, and layered structures have been synthesized with various design motifs and porosities.[1,4−6] Arising from their singular architecture, these materials have been shown to possess a unique confluence of chemical, optical, and physical properties.[2,7−10] For example, their high porosities make them ideal candidates for applications such as materials for photoelectrodes and particularly for gas adsorption and hydrogen storage, thus promoting the production of clean fuels for automobiles and reduction of carbon monoxide emission.[2,11−15] Furthermore, the choice of the organic monomers can be used to control the shape and size of the one-dimensional laminar pores, providing a large design space to engineer their microstructure at the level of the organic building blocks from a bottom-up approach. Paramount in advancing 2D COFs for the various types of applications, however, is the complete understanding of how their mechanical and thermal properties vary with their modular microstructures.

In terms of the understanding of thermal transport in porous crystals in general, studies have mainly focused on metal−organic frameworks (MOFs).[16−22] It is questionable, however, whether insights gained from these works are transferable to their COF cousins. While both COFs and MOFs have open nanopores as a common feature, they are vastly different from both chemical and structural perspectives. For instance, COFs are mainly made up of light atoms held together by strong covalent bonds, whereas MOFs contain atomic species with large masses and ionic bonding. Moreover, 2D COFs are

Received: November 5, 2021
Accepted: February 2, 2022
Published: February 10, 2022

https://doi.org/10.1021/acsnano.1c09833
ACS Nano 2022, 16, 2843−2851

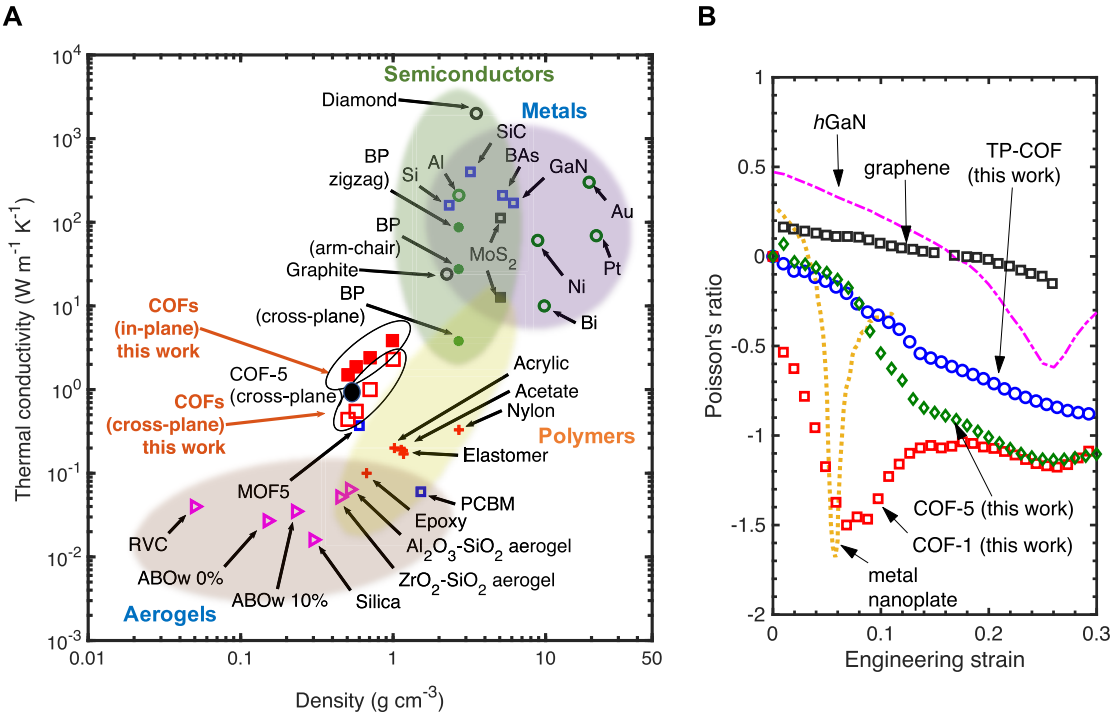

Figure 1. (a) Comparison of room-temperature thermal conductivity as a function of density for our COF structures with common aerogels, polymers, and metallic and nonmetallic solids.[25−30] Also included is our recent experimental measurement of cross-plane thermal conductivity of thin-film COF-5 (black solid circle). For comparison, MD-predicted thermal conductivity for MOF-5 is also included.[31] In general, higher mass densities are associated with higher thermal conductivities. The thermal conductivity of COFs, however, marks a regime of materials design that combines low densities with high thermal conductivities. (b) Comparison of the Poisson's ratio as a function of applied strain for a carbon honeycomb structure,[32] *h*-GaN,[33] graphene,[33] metal nanoplates,[34] and our COFs. In comparison to the other auxetic materials, large negative Poisson's ratios are calculated for our COFs that result from the swiveling motion of the organic linkers. The negative Poisson's ratio of our COFs can also be tuned based on the pore size.

assembled by covalently bonded organic building units in the in-plane direction, with van der Waals interactions holding the layers together in the cross-plane direction, which provides an intrinsic anisotropy in their chemical and structural properties. This is particularly useful for applications such as ion and gas transport through the laminar pores and for drug delivery.[23] These unique features separate COFs from other materials and position them as one of the premier materials with unique combinations of exceptional chemical, optical, and physical properties arising from their remarkable architecture.[2,7−10] We recently measured the thermal conductivity of 2D COF-5 thin films through thermoreflectance experiments and revealed that this material possesses one of the highest thermal conductivity-to-density ratios of any material reported to date with their equivalent porosity and mass density.[24] In this work, through atomistic simulations, we demonstrate that through the proper design of their pore geometries, the thermal conductivities of 2D COFs can be tuned over a large range (from ∼0.5 to 5 W m^{-1} K^{-1}), marking a direction for low-density materials (spanning the range of 0.5−1 g cm^{-3}) with increased thermal conductivities as shown in Figure 1a.

Similar to their thermal properties, an in-depth study of the mechanical properties of 2D COFs is also nonexistent in prior literature. Herein, we reveal that these materials possess a very unique response to mechanical strain by showing auxetic behavior with very high negative Poisson's ratio (reaching values of around −1.5). This finding is in contrast to most materials that shrink laterally when stretched in the orthogonal direction and are characterized by a positive Poisson's ratio with a usual value of around 0.33. Although rare, materials with a negative Poisson's ratio (a.k.a. auxetic materials) that counterintuitively expand laterally in response to an orthogonal tensile force as allowed by thermodynamics,[35−41] are accompanied by anomalous and usually enhanced physical properties such as enhanced toughness and higher sound and vibration absorption capabilities.[42−47] Motivated by their intriguing physical properties in conjunction with their widespread applications in fields ranging from medicine and tissue engineering to aerospace and defense,[48−51] auxetic behavior has been verified for open cell foams and honeycomb structures,[44,52] cubic metals strained along nonaxial directions,[46,53] two-dimensional materials such as graphene and hexagonal boron nitride,[33,54,55] molecular structures such as zeolites and polymer networks,[37−39,56,57] and a few metal−organic frameworks.[58,59] For most of these auxetic materials, however, achieving highly negative Poisson's ratios (lower than −0.3, as found in most auxetic materials) with the added advantage of tunability in their mechanical properties over a wide range through precise control over the microstructure has remained an elusive task. In this work, by systematically studying prototypical 2D COFs, we show that the mechanical properties (such as the negative Poisson's ratio and the Young's modulus) of 2D COFs can be tuned across a wide range by the proper bottom-up design of their microstructure. Our results show that the swiveling motion of the functional groups leads to an auxetic behavior quantified by a high negative Poisson's ratio in comparison to other auxetic materials such as hexagonal GaN, graphene, and metal nanoparticles as shown in Figure 1b.[32,33,33] Taken together, our results show that the porosity of COFs can be used to

https://doi.org/10.1021/acsnano.1c09833
ACS Nano 2022, 16, 2843−2851

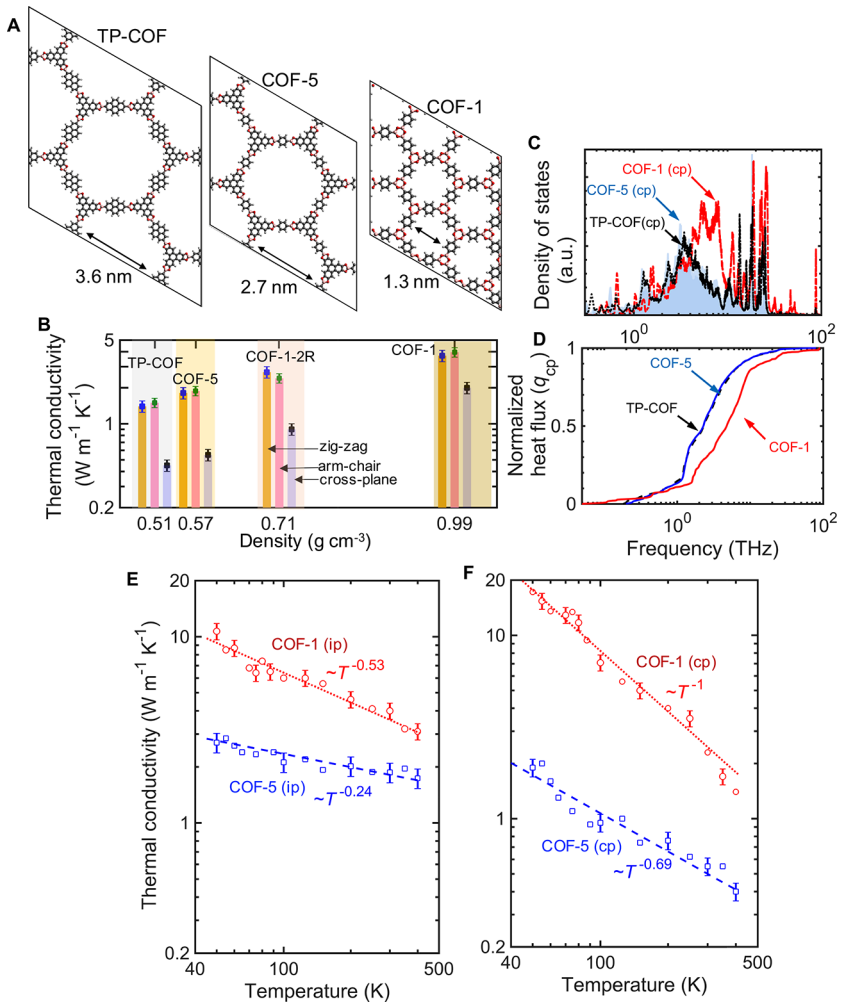

Figure 2. (a) Schematic illustration of the molecular structures of the COFs studied in this work. The gray, white, red, and pink atoms represent carbon, hydrogen, boron, and oxygen. (b) Thermal conductivity in the three principle directions for the COFs as a function of their density. (c) Vibrational density of states in the cross-plane direction for the three COFs. The density of states for the TP-COF and COF-5 structures are similar for the entire frequency range, whereas the vibrational density of states is comparatively larger in the 1−10 THz range for COF-1. (d) Normalized thermal conductivity accumulation in the cross-plane direction. Temperature-dependent thermal conductivity in the (e) in-plane and (f) cross-plane directions for COF-1 and TP-COF.

manipulate both their thermal and mechanical properties, setting them up as an emerging class of modular nanomaterials with multifunctional characteristics.

RESULTS AND DISUCUSSION

We base our calculations on three 2D COFs that vary in their porosities and internal architectures, as shown in Figure 2a. We note that although we refer to our structures as "2D COFs" (as is the convention to describe these polymers), the layering in the cross-plane plane (the *z*-direction) results in 3D structures with laminar pore channels. Among the three structures, COF-1 possesses the highest density (almost twice that of TP-COF; see Figure 2b), the smallest porosity, and a pore diameter of ∼1.3 nm. The TP-COF structure has the largest porosity of the three structures with a ∼33% larger pore diameter as compared to that of COF-5. However, because of its larger aromatic surface as compared to COF-5 (with only 1 phenyl ring as the linker), the overall density of the TP-COF and COF-5 structures differ by only ∼12%. This similarity allows us to study the effect of the linker size on the mechanical and thermal properties, as discussed below. Furthermore, to investigate the effect of varying porosity while maintaining similar internal microstructure, we modified the COF-1 structure by adding a phenyl ring to the linkers (see Figure S5 for the COF-1-2R structure, where "R" stands for "rings"). The simulations are performed with the LAMMPS package.[60] All details, including the computational domain setups and the subsequent equilibration procedures, are provided in Methods and the Supporting Information.

We calculate the thermal conductivities of our COFs in the two in-plane directions (zigzag and arm-chair) and also in the cross-plane direction (or the *z*-direction) from equilibrium molecular dynamics (EMD) simulations (see Figure S1). Our EMD-predicted thermal conductivities as a function of mass density are shown in Figure 2b. The thermal conductivity in the zigzag and arm-chair directions are within the simulation error for a particular COF. The thermal conductivities in the cross-plane direction with weaker van der Waals interactions are lower in comparison to the thermal conductivities in the in-plane directions with the stronger covalent bonds for all four COFs. The thermal conductivity in the in-plane and cross-plane directions for the COFs scale with density as shown in

https://doi.org/10.1021/acsnano.1c09833
ACS Nano 2022, 16, 2843−2851

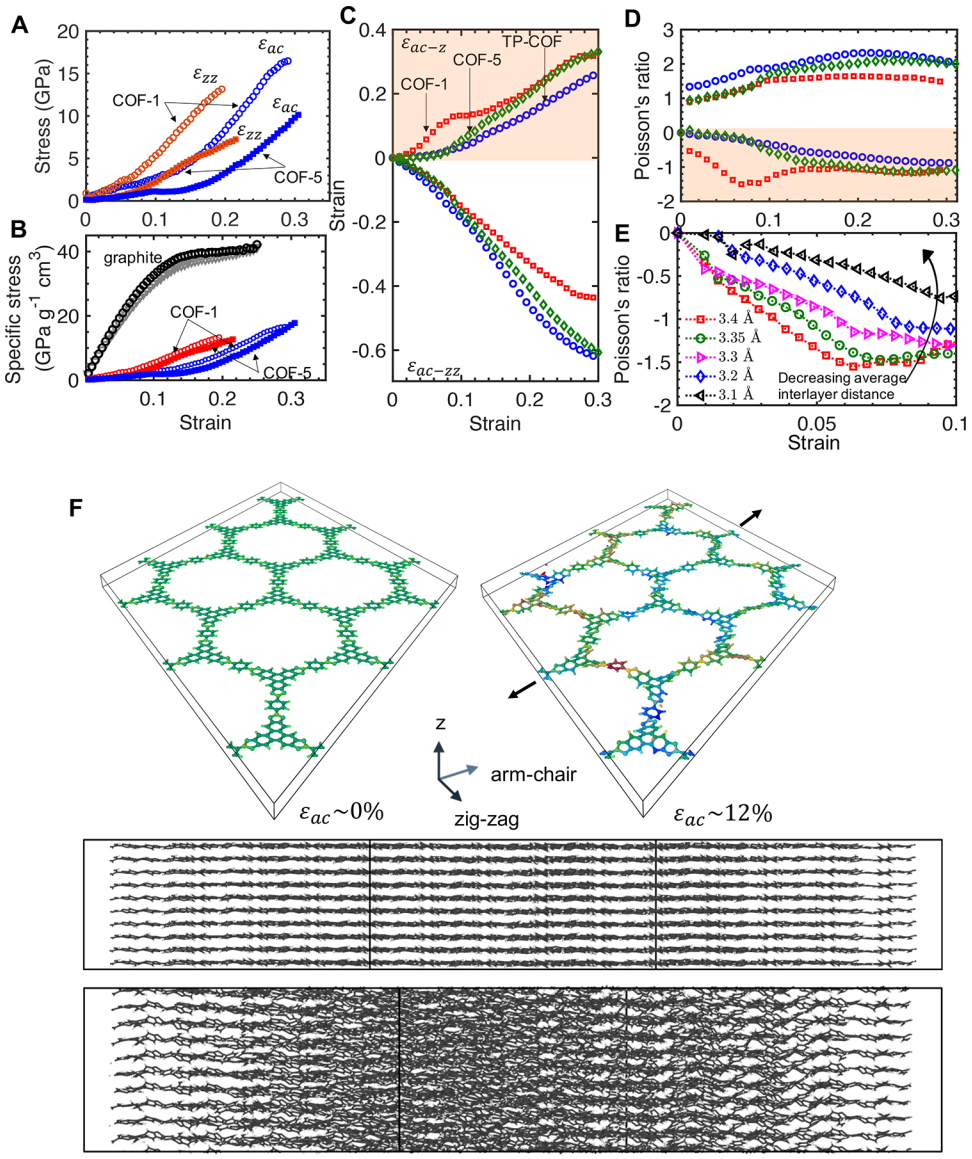

Figure 3. (a) Stress versus strain curves for uniaxial tensile loading in the in-plane directions for COF-1 and COF-5. (b) Specific stress (normalized by density) versus strain for the COFs. For comparison, the mechanical response of graphite (a similar van der Waals solid) is also shown. (c) The resultant strain in the cross-plane and zigzag directions versus the applied strain in the arm chair direction for the three COFs. (d) The Poisson's ratio extracted from the molecular dynamics simulations, which shows negative values in the cross-plane direction for all three COFs. The Poisson's ratio is highly negative in the initial tensile phase (<5% strain) because of the highly nonlinear strain induced in this regime. (e) The Poisson's ratio for COF-1 with varying average interlayer separation from 3.4 to 3.1 Å. (f) Snapshots of the COF-5 structure showing atoms and bonds colored according to their *z*-coordinate.

Figure 2b. Even though the pores of TP-COF are larger than that of COF-5, the similarities in the mass densities and the vibrational density of states (DOS) between the two structures, as shown in Figure 2c for the cross plane direction, result in an overall similar thermal conductivity between TP-COF and COF-5. Furthermore, the spectral contributions to thermal conductivity between the two structures are essentially identical, as shown in Figure 2d, where we plot the spectrally decomposed heat flux accumulation for TP-COF, COF-5, and COF-1 in the cross-plane direction. The DOS and spectral heat flux accumulation for COF-1 and COF-1-2R are similar for both in-plane and cross-plane directions as shown in Figure S8. Although the vibrations span a large frequency spectrum (up to and greater than 50 THz), it is interesting to note that >90% of the heat is carried by vibrations below 10 THz for all structures in the cross-plane direction (see Figure 2d). However, in the in-plane direction, modes greater than 10 THz have relatively higher contributions (as shown in Figures S7 and S8). This could be due to the anisotropic nature of bonding in 2D COFs where strong covalent bonds are found within a 2D layer, whereas the relatively weaker nonbonded interactions hold the 2D sheets together in the cross-plane direction. In comparison to the structures with lower mass density, the spectrally decomposed heat accumulation for COF-1 shifts to higher frequencies in the 1−10 THz range, which is in line with the larger DOS of the COF-1 structure in this frequency range (see Figure 2c).

Panels e and f of Figure 2 show the temperature-dependent thermal conductivities for COF-1 and COF-5 in the in-plane and cross-plane directions, respectively. The temperature-

https://doi.org/10.1021/acsnano.1c09833
ACS Nano 2022, 16, 2843−2851

dependent thermal conductivity of TP-COF is plotted in Figure S4 for clarity because the values are similar to that of COF-5. In general, for defect-free, dielectric crystalline materials, the temperature dependence of thermal conductivity is mainly dictated by anharmonic phonon−phonon scattering processes.[61,62] Stronger anharmonicity leads to a stronger temperature dependence. Therefore, the stronger temperature dependence in the cross-plane direction for the COFs as compared to the in-plane direction suggests that anharmonicity has a larger contribution along the cross-plane direction. Moreover, the temperature trends for the COF-1 structure also suggest that anharmonic processes are more pronounced in structures with higher mass densities. It is important to note that our results are based on classical molecular dynamics simulations. As such, all the available modes (including the relatively higher frequency vibrations that would likely not participate at lower temperatures when quantum effects are considered) are activated for the entire temperature range studied in this work. Even though the higher-frequency modes have a relatively lower contribution to the total cross-plane heat conduction, these modes could still be involved in vibrational scattering.

As mechanical properties are intimately related to thermal properties, we build a holistic picture of our COFs by studying their mechanical properties, which are summarized in Figure 3. Additional details regarding the deformation simulations are given in Methods. Figure 3a shows the stress−strain curves resulting from uniaxial tension in the arm-chair and zigzag directions for COF-1 and COF-5. Overall, the uniaxial stress−strain curves are highly nonlinear with a Young's modulus that gradually increases with strain (see Figure S15). The nonlinearity can be understood as a result of the bending of the pore walls that increases with increasing tension, leading to the decrease in the pore volume (see Figures S18−S20). Although the failure strain largely remains the same for the COFs, it decreases as the pore size increases as demonstrated in Figure 3a. Similar to the changes in thermal conductivities for the different COFs, the Young's moduli and ultimate tensile stresses also scale with the density of the COFs (as shown in Figures S15−S17). It is also interesting to note that unlike the similar values of thermal conductivities in the zigzag and arm-chair directions for a particular COF, there is a large anisotropy in the uniaxial stress−strain behavior in the two directions; the Young's modulus is higher for initial strain (up to 10%) when uniaxial tension is applied in the arm-chair direction as compared to the case where uniaxial tension is applied in the zigzag direction (see Figure S15).

The nonlinear stress−strain behavior of the COFs is in contrast to the mechanical response of graphite, which has a similar 2D layered structure held together by van der Waals forces. In Figure 3b, we compare the specific stress (normalized by density) as a function of strain for our representative COFs to that of graphite. Overall, graphite has a much larger stiffness and is intrinsically stronger than the porous COF structures. However, the relatively more compliant nature of the COFs results in highly negative Poisson's ratios for these materials, as we discuss in detail below.

We investigate the overall change in the structure of our COF domains with the application of tensile strain (as quantified by the Poisson's ratio, ν) by plotting the strain in the zigzag and cross-plane directions during uniaxial deformation in the arm-chair direction in Figure 3c. For all COFs, the length of the computational domain shrinks in the zigzag direction (as represented by the negative strain), whereas the computational domains expand in the cross-plane direction. Furthermore, a strongly nonlinear behavior is observed both in the cross-plane and zigzag directions during the initial ∼10% of applied strain for the COF-1 structure.

The resulting Poisson's ratios in the zigzag ($\nu_{ac\text{-}zz} = -\partial\varepsilon_{zz}/\partial\varepsilon_{ac}$) and cross-plane ($\nu_{acz} = -\partial\varepsilon_{z}/\partial\varepsilon_{ac}$) directions due to the uniaxial tensile deformation in the arm-chair direction are shown in Figure 3d. The Poisson's ratio are much higher during the initial nonlinear behavior for COF-1, reaching a minimum value of $\nu_{ac\text{-}z} \approx -1.8$ at ∼8% strain. A relatively constant value of −1 for Poisson's ratio is observed at higher applied strains. The mechanism for the overall negative Poisson's ratio derives from the extension of the bonds in the linkers between the aromatic phenyl rings, which forces the rings to swivel and twist from their almost parallel equilibrium positions, thus forcing the neighboring chains further apart because of the van der Waals repulsive forces. To support this idea, we conduct additional simulations for our COF-1 structure by decreasing the equilibrium van der Waals repulsive forces and perturbing the interlayer separations from 3.4 to 3.1 Å. The Poisson's ratios predicted for these structures are shown in Figure 3e, which shows that as the repulsive forces and the interlayer separation decrease, the Poisson's ratio can be lowered drastically for the COF-1 structures. This finding shows that along with the modular geometries between the different COF structures, variations in the interlayer distances can also lead to changes in the Poisson's ratio of these materials.

To further investigate the molecular-level mechanisms responsible for the negative Poisson's ratio of our COFs, we studied the internal structures of our COFs during the tensile deformation process. Figure 3f shows the COF-5 structure with atoms and bonds colored corresponding to their z-coordinate (cross-plane direction) for the initially equilibrated domain (left panel) and the domain at an applied strain of 12% in the arm-chair direction (right panel). The bottom panel shows the corresponding views along the cross-plane direction for the two strains. For the unstrained case (top panel), the aromatic rings are aligned roughly parallel to the tensile axis. However, as the strain increases, the aromatic rings are perturbed from their equilibrium positions because the lateral forces due to the van der Waals interactions are not strong enough to prevent the mechanical reorientation of the aromatic rings. Similar color maps showing further strain levels for all COFs are presented in the Supporting Information (Figures S18−S20). Upon comparison of the relative degrees of "swiveling" of the molecular linkers between the three COFs, a larger amount of twisted aromatic linkers that are almost positioned normal to the tensile axis in the COF-1 and COF-1-2R structures leads to the higher negative Poisson's ratio among the four COFs studied in this work.

To investigate the effect of strain on the thermal conductivity of our COFs, we plot the normalized thermal conductivities (with respect to the cross-plane thermal conductivity of unstrained COF-1) in all three directions for COF-1 in Figure 4a to emphasize the change in the anisotropic thermal conductivity with applied strain. The thermal conductivity in the cross-plane direction decreases monotonically with applied tensile strain for our COF-1 structure. The thermal conductivity along the tensile axis, however, increases with applied strain, while a reduction in thermal conductivity is

https://doi.org/10.1021/acsnano.1c09833
ACS Nano 2022, 16, 2843−2851

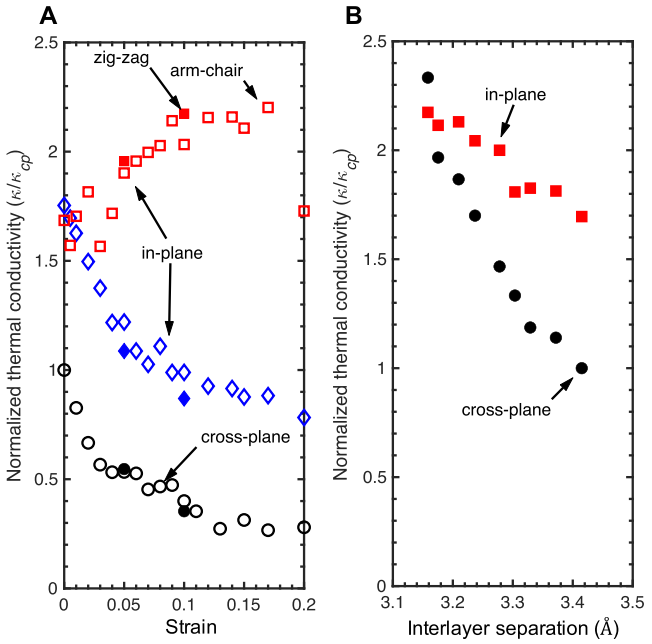

Figure 4. (a) Thermal conductivity of COF-1 as a function of uniaxial tension. The hollow symbols represent the structure when stretched in the arm-chair direction, and the solid symbols represent the structure when stretched in the zigzag direction. (b) Thermal conductivity of COF-1 as a function of average interlayer separation distance between the 2D layers. We note that the baseline interlayer separation defined by the interatomic potential is 3.4 Å.

observed in the orthogonal in-plane direction where the computational domain shrinks (with a positive Poission's ratio). This result shows that although there is considerable out-of-plane distortions of the atoms due to uniaxial tension, the application of tensile strain results in a relatively better alignment of the atoms along the tensile axis as compared to the other two orthogonal directions, thus leading to a better heat conduction in that direction. Therefore, along with the high negative Poisson's ratio, uniaxial tension can also be used to increase the anisotropy in the thermal properties of 2D COFs (as seen by the more than 6× difference in the in-plane and cross-plane thermal conductivities for our COF-1 structure as shown in Figure 4a).

The cross-plane thermal conductivity of COF-1 decreases by almost an order of magnitude with the application of large uniaxial strain in the in-plane direction, which also induces similar strain levels in the cross-plane direction (see Figure 3c). This result suggests that controlling the interlayer separation can lead to large modifications in the thermal properties and that strain engineering can be used to manipulate the anisotropic thermal conductivity. This effect is demonstrated in Figure 4b, where we show the effect of varying interlayer separation on the in-plane and cross-plane thermal conductivities for the COF-1 structure. Bringing the layers closer together can drastically increase the thermal conductivity; decreasing the separation by ∼10% can lead to a 100% increase in cross-plane thermal conductivity of COF-1. The thermal conductivity in the in-plane directions also increase monotonically as the layer separation is decreased. This could possibly be due to the higher degree of confinement of the out-of-plane motion of the atoms. Detailed analyses of these phenomena are beyond the scope of this work but deserve further investigation, which we leave for future work.

To better relate the mechanical strain response to the variation in the anisotropic thermal properties of 2D COFs, we calculate the von Mises strain associated with each atom at different strain levels (as calculated in ref 63). Panels a and b of Figure 5 show the local strain where the atoms are colored

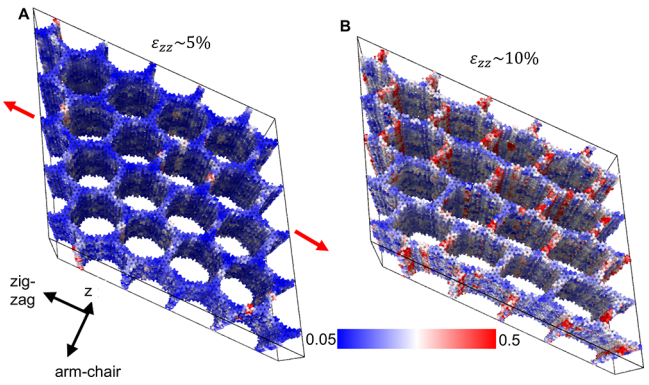

Figure 5. Snapshots of the computational domains showing calculations of atomic-level strain relative to the relaxed structure for COF-5 at (a) ε = 0.05 and (b) ε = 0.10 under uniaxial tension along the zigzag direction. As the tensile strain is increased, stress localization (represented by the red colored atoms) is mainly observed along the arm-chair direction, whereas the polymer chains align better along the tensile axis because of stretching.

based on their von Mises strain under 5% and 10% uniaxial strain in the zigzag direction, respectively. As uniaxial strain is increased in the zigzag direction, stress localization is comparably higher along the arm-chair direction where the computational domain shrinks. This is evident from the higher concentration of the red colored atoms in the computational domain that are mainly located along the arm-chair direction, suggesting that the swiveling and twisting motion of the aromatic rings leads to higher stress states in that direction as shown in Figure 5b. Along the direction of the applied strain, the polymer chain stretching leads to a relatively better orientation of the polymer building blocks (see Figure S22). This manifests in a higher thermal conductivity along the tensile axis, whereas stress localization likely leads to lower thermal conductivities in the other two orthogonal directions (see Figure 4a). Along the arm-chair and the cross-plane directions, where the polymer chains lack orientational order because of the stress localization, enhanced vibrational scattering leads to the monotonically decreasing thermal conductivity with increasing tensile strain. Furthermore, even though the lattice shrinks along the arm-chair direction with a positive Poisson's ratio because of tensile strain along the zigzag direction, the polymer chains are forced apart in the nonbonded direction because of stress localization and reorientation of the aromatic rings resulting in the auxetic behavior in the cross-plane direction. Therefore, through the control of the local lattice deformation (and stress localization) with uniaxial tensile force, the anisotropic thermal conductivity along with the mechanical response can also be manipulated in these 2D polymers.

Comparing the thermal conductivities of our COFs with other classes of materials as a function of mass density elucidates their unique thermal performance, as shown in Figure 1a. We also include the experimentally measured cross-

https://doi.org/10.1021/acsnano.1c09833
ACS Nano 2022, 16, 2843−2851

plane thermal conductivity (at room temperature) of a thin-film 2D COF-5 from our previous work in Figure 1a.[24] However, we caution against a quantitative comparison between our MD predictions and the experimentally determined thermal conductivity because of the insufficiencies of the interatomic potential used to describe our models based on the AIREBO potential and the classical nature of MD simulations where quantum effects are ignored. In general, the thermal conductivity of materials gradually increases with increasing density. Metals and crystalline semiconductors usually possess high thermal conductivity with high mass densities. The fully dense 2D materials such as MoS_2 and BP follow this trend because they usually possess high thermal conductivities (mainly in the in-plane direction) along with relatively high mass densities. While the densities of our COFs, along with the densities of a similar metal−organic framework (MOF-5) are comparable to the densities of aerogels, their thermal conductivities (for most cases) are more than an order of magnitude greater than those of aerogels and other porous materials, marking a regime of materials design that combines low densities with relatively higher thermal conductivities. This regime could potentially lead to structural materials with ultralightweight characteristics[64,65] Moreover, the introduction of guest atoms and molecules could also have a large impact on their physical properties as has been previously observed for porous crystals.[12,16,22,66−68]

Along with the exceptional thermal properties of 2D COFs, comparing our MD-predicted Poisson's ratio to computational predictions of Poisson's ratios for *h*-GaN and graphene that have similar 2D structures with van der Waals interactions between the layers sheds light on their unique mechanical response to uniaxial tension in Figure 1b. The auxeticity that arises at a critical strain in these 2D honeycomb structures has been ascribed to the anomalous variation in bond angles.[33] Similarly, auxeticity in metallic nanoplates, which are not observed in the bulk counterparts, have been demonstrated based on surface or edge effects.[34] However, these mechanisms are very different than the molecular swiveling mechanism observed for our COFs, which can lead to a larger auxeticity as shown for our nanoporous (and layered) COF structures. In general, the auxetic behavior observed for our COFs also differs fundamentally from the re-entrant mechanism based on classical mechanics of angular rotation of cell walls that dictates the negative Poisson's effect for honeycomb structures and open cell foams.[36,44] The drastically different mechanistic approach to manipulating the negative mechanical response for COFs leads to their larger and more dynamic negative Poisson's ratio as shown in Figure 1b.

CONCLUSIONS

In summary, we performed systematic atomistic simulations to reveal that COFs mark a regime of materials' design that combines low densities with unusually high thermal conductivities and high negative Poisson's ratio that can be tailored through carefully engineering their microstructure. Their singular layered structure results in anisotropy in thermal conductivity, which can be further enhanced through the swiveling motion of the organic linkers under uniaxial tensile strain. This swiveling motion also leads to an auxetic behavior quantified by a high negative Poisson's ratio in comparison to other auxetic materials. Our results show that the porosity of COFs can be used to manipulate both their thermal and mechanical properties, setting them up as an emerging class of multifunctional materials.

METHODS

Our molecular dynamics (MD) simulations utilize the adaptive intermolecular reactive empirical bond order (AIREBO) potential to describe the interatomic interactions.[69] The potential describes only the interactions between and within carbon and hydrogen atoms. As such, our models are strictly made up of carbon atoms and do not include boron, oxygen, and nitrogen atoms as in the real COF-5 systems. However, we do use the correct masses for the boron, oxygen, and nitrogen atoms in our computational domains. For all simulations, the computational domains are equilibrated under the Nose−Hoover thermostat and barostat[70] (which is the *NPT* integration with the number of particles, pressure and temperature of the system held constant) for a total of 2 ns at 0 bar pressure with a time step of 0.5 fs throughout the simulations. Following the *NPT* integration, an *NVT* integration (with constant volume and number of particles) is utilized to equilibrate the COFs at the desired temperature of the simulations. Note that we apply periodic boundary conditions in all directions for all our simulations. Figure S1a of the Supporting Information shows an example of our COF-5 structure equilibrated using the procedure outlined above. We also vary the total cross-plane thickness, *d*, and length of the computational domain, *L*, to check for system size effects for our nonequilibrium and equilibrium MD simulations to predict the thermal properties as detailed in the Supporting Information.

To assess the mechanical properties, a uniaxial deformation in the zigzag or arm-chair direction is applied at a strain rate of 10^8 s^{-1}. The other periodic boundaries are held at 0 bar (or "stress-free" conditions) under the *NPT* integration. The stress and strain along all three directions are calculated every 0.1 ps to generate the stress−strain relationships for the COFs.

After equilibration, the thermal conductivities of our COFs at different temperatures are predicted via the Green−Kubo (GK) approach under the equilibrium MD framework. In this formalism, the thermal conductivities of our COFs along the zigzag (zz-), arm-chair (ac-) and cross-plane (*z*-) directions are calculated as

$$\kappa_{zz,ac,z} = \frac{1}{k_B V T^2} \int_0^\infty \langle S_{zz,ac,z}(t) S_{zz,ac,z}(0) \rangle \, dt \quad (1)$$

Here *t* is time; *T* and *V* are the temperature and volume of the systems, respectively; and $\langle S_{zz,ac,z}(t)\, S_{zz,ac,z}(0) \rangle$ is the component of the heat current autocorrelation function (HCACF) in the prescribed directions. To ensure that the HCACF decays to zero (and crosses zero several times), we set the total correlation time period for the integration of the HCACF to 50 ps as shown in the inset of Figure S1b of the Supporting Information. The heat current is computed every 10 time steps during the data collection period followed by integration of the heat current to calculate the converged thermal conductivity for our COFs. The converged thermal conductivity is determined from the integration as shown in Figure S1b of the Supporting Information (dashed line) for our COF-5 structure.

ASSOCIATED CONTENT

Supporting Information

The Supporting Information is available free of charge at https://pubs.acs.org/doi/10.1021/acsnano.1c09833.

Details of the computational domain setup, equilibrium and nonequilibrium molecular dynamics approaches, vibrational density of states calculations, and heat flux calculations (PDF)

AUTHOR INFORMATION

Corresponding Authors

Ashutosh Giri − *Department of Mechanical, Industrial and Systems Engineering, University of Rhode Island, Kingston,*

https://doi.org/10.1021/acsnano.1c09833
ACS Nano 2022, 16, 2843−2851

Rhode Island 02881, United States; orcid.org/0000-0002-8899-4964; Email: ashgiri@uri.edu

Patrick E. Hopkins − *Department of Mechanical and Aerospace Engineering, University of Virginia, Charlottesville, Virginia 22904, United States; Department of Materials Science and Engineering and Department of Physics, University of Virginia, Charlottesville, Virginia 22904, United States*; Email: phopkins@virginia.edu

Authors

Austin M. Evans − *Department of Chemistry, Columbia University, New York City, New York 10027, United States;* orcid.org/0000-0002-3597-2454

Muhammad Akif Rahman − *Department of Mechanical, Industrial and Systems Engineering, University of Rhode Island, Kingston, Rhode Island 02881, United States*

Alan J. H. McGaughey − *Department of Mechanical Engineering, Carnegie Mellon University, Pittsburgh, Pennsylvania 15213, United States; Department of Materials Science and Engineering, Carnegie Mellon University, Pittsburgh, Pennsylvania 15213, United States;* orcid.org/0000-0002-0118-6893

Complete contact information is available at: https://pubs.acs.org/10.1021/acsnano.1c09833

Notes

The authors declare no competing financial interest.

ACKNOWLEDGMENTS

This work is supported by the Office of Naval Research, Grant Nos. N00014-21-1-2622 and N00014-20-1-2686. The work is also partially supported by the National Science Foundation (NSF Award No. 2119365 and NSF Award DMR-2025013). A.M.E. is supported by the Schmidt Science Fellows, in partnership with the Rhodes Trust.

REFERENCES

(1) Evans, A. M.; Parent, L. R.; Flanders, N. C.; Bisbey, R. P.; Vitaku, E.; Kirschner, M. S.; Schaller, R. D.; Chen, L. X.; Gianneschi, N. C.; Dichtel, W. R. Seeded growth of single-crystal two-dimensional covalent organic frameworks. *Science* **2018**, *361*, 52−57.

(2) Bisbey, R. P.; Dichtel, W. R. Covalent Organic Frameworks as a Platform for Multidimensional Polymerization. *ACS Central Science* **2017**, *3*, 533−543.

(3) Diercks, C. S.; Yaghi, O. M. The atom, the molecule, and the covalent organic framework. *Science* **2017**, *355*, No. eaal1585.

(4) Servalli, M.; Schlüter, A. D. Synthetic Two-Dimensional Polymers. *Annu. Rev. Mater. Res.* **2017**, *47*, 361−389.

(5) Grill, L.; Dyer, M.; Lafferentz, L.; Persson, M.; Peters, M. V.; Hecht, S. Nano-architectures by covalent assembly of molecular building blocks. *Nat. Nanotechnol.* **2007**, *2*, 687.

(6) Liang, R.-R.; Jiang, S.-Y.; A, R.-H.; Zhao, X. Two-dimensional covalent organic frameworks with hierarchical porosity. *Chem. Soc. Rev.* **2020**, *49*, 3920−3951.

(7) Waller, P. J.; Lyle, S. J.; Osborn Popp, T. M.; Diercks, C. S.; Reimer, J. A.; Yaghi, O. M. Chemical Conversion of Linkages in Covalent Organic Frameworks. *J. Am. Chem. Soc.* **2016**, *138*, 15519−15522.

(8) Lohse, M. S.; Stassin, T.; Naudin, G.; Wuttke, S.; Ameloot, R.; De Vos, D.; Medina, D. D.; Bein, T. Sequential Pore Wall Modification in a Covalent Organic Framework for Application in Lactic Acid Adsorption. *Chem. Mater.* **2016**, *28*, 626−631.

(9) Côté, A. P.; Benin, A. I.; Ockwig, N. W.; O'Keeffe, M.; Matzger, A. J.; Yaghi, O. M. Porous, Crystalline, Covalent Organic Frameworks. *Science* **2005**, *310*, 1166−1170.

(10) Xu, H.; Gao, J.; Jiang, D. Stable, crystalline, porous, covalent organic frameworks as a platform for chiral organocatalysts. *Nat. Chem.* **2015**, *7*, 905.

(11) Sick, T.; Hufnagel, A. G.; Kampmann, J.; Kondofersky, I.; Calik, M.; Rotter, J. M.; Evans, A.; Döblinger, M.; Herbert, S.; Peters, K.; Böhm, D.; Knochel, P.; Medina, D. D.; Fattakhova-Rohlfing, D.; Bein, T. Oriented Films of Conjugated 2D Covalent Organic Frameworks as Photocathodes for Water Splitting. *J. Am. Chem. Soc.* **2018**, *140*, 2085−2092. PMID: 29249151

(12) Giri, A.; Hopkins, P. E. Heat Transfer Mechanisms and Tunable Thermal Conductivity Anisotropy in Two-Dimensional Covalent Organic Frameworks with Adsorbed Gases. *Nano Lett.* **2021**, *21*, 6188−6193.

(13) Han, S. S.; Furukawa, H.; Yaghi, O. M.; Goddard, W. A. Covalent Organic Frameworks as Exceptional Hydrogen Storage Materials. *J. Am. Chem. Soc.* **2008**, *130*, 11580−11581.

(14) Furukawa, H.; Yaghi, O. M. Storage of Hydrogen, Methane, and Carbon Dioxide in Highly Porous Covalent Organic Frameworks for Clean Energy Applications. *J. Am. Chem. Soc.* **2009**, *131*, 8875−8883.

(15) Amirjalayer, S.; Snurr, R. Q.; Schmid, R. Prediction of Structure and Properties of Boron-Based Covalent Organic Frameworks by a First-Principles Derived Force Field. *J. Phys. Chem. C* **2012**, *116*, 4921−4929.

(16) Babaei, H.; McGaughey, A. J. H.; Wilmer, C. E. Effect of pore size and shape on the thermal conductivity of metal-organic frameworks. *Chem. Sci.* **2017**, *8*, 583−589.

(17) Babaei, H.; Wilmer, C. E. Mechanisms of Heat Transfer in Porous Crystals Containing Adsorbed Gases: Applications to Metal-Organic Frameworks. *Phys. Rev. Lett.* **2016**, *116*, 025902.

(18) Han, L.; Budge, M.; Alex Greaney, P. Relationship between thermal conductivity and framework architecture in MOF-5. *Comput. Mater. Sci.* **2014**, *94*, 292−297. IWCMM23 Special Issue

(19) Huang, B. L.; McGaughey, A. J. H.; Kaviany, M. Thermal conductivity of metal-organic framework 5 (MOF-5): Part I. Molecular dynamics simulations. *Int. J. Heat Mass Transfer* **2007**, *50*, 393−404.

(20) Wieme, J.; Vandenbrande, S.; Lamaire, A.; Kapil, V.; Vanduyfhuys, L.; Van Speybroeck, V. Thermal Engineering of Metal−Organic Frameworks for Adsorption Applications: A Molecular Simulation Perspective. *ACS Appl. Mater. Interfaces* **2019**, *11*, 38697−38707.

(21) Babaei, H.; McGaughey, A. J. H.; Wilmer, C. E. Transient Mass and Thermal Transport during Methane Adsorption into the Metal−Organic Framework HKUST-1. *ACS Appl. Mater. Interfaces* **2018**, *10*, 2400−2406.

(22) Babaei, H.; DeCoster, M. E.; Jeong, M.; Hassan, Z. M.; Islamoglu, T.; Baumgart, H.; McGaughey, A. J. H.; Redel, E.; Farha, O. K.; Hopkins, P. E.; Malen, J. A.; Wilmer, C. E. Observation of reduced thermal conductivity in a metal-organic framework due to the presence of adsorbates. *Nat. Commun.* **2020**, *11*, 4010.

(23) Liang, X.; Tian, Y.; Yuan, Y.; Kim, Y. Ionic Covalent Organic Frameworks for Energy Devices. *Adv. Mater.* **2021**, *33*, 2105647.

(24) Evans, A. M. Thermally conductive ultra-low-k dielectric layers based on two-dimensional covalent organic frameworks. *Nat. Mater.* **2021**, *20*, 1142.

(25) Slack, G. Nonmetallic crystals with high thermal conductivity. *J. Phys. Chem. Solids* **1973**, *34*, 321−335.

(26) Field, J. E. *The Properties of Natural and Synthetic Diamond*; Academic Press, London, 1992.28602602

(27) Harris, G. *Properties of silicon carbide*; INSPEC: London, 1995.

(28) Lide, D. R. *CRC Handbook for Chemistry and Physics*, internet ver.; CRC Press/Taylor and Francis: Boca Raton, FL, 2008.

(29) Ross, R. B. *Metallic Materials Specification Handbook*, 4th ed.; Springer, 1992.

(30) Chiritescu, C.; Cahill, D. G.; Nguyen, N.; Johnson, D.; Bodapati, A.; Keblinski, P.; Zschack, P. Ultralow Thermal Conductivity in Disordered, Layered WSe2 Crystals. *Science* **2007**, *315*, 351−353.

(31) Huang, B. L.; Ni, Z.; Millward, A.; McGaughey, A. J. H.; Uher, C.; Kaviany, M.; Yaghi, O. Thermal conductivity of a metal-organic framework (MOF-5): Part II. Measurement. *Int. J. Heat Mass Transfer* **2007**, *50*, 405−411.
(32) Pang, Z.; Gu, X.; Wei, Y.; Yang, R.; Dresselhaus, M. S. Bottom-up Design of Three-Dimensional Carbon-Honeycomb with Superb Specific Strength and High Thermal Conductivity. *Nano Lett.* **2017**, *17*, 179−185. PMID: 28073254
(33) Qin, G.; Qin, Z. Negative Poisson's ratio in two-dimensional honeycomb structures. *npj Computational Materials* **2020**, *6*, 51.
(34) Ho, D. T.; Park, S.-D.; Kwon, S.-Y.; Park, K.; Kim, S. Y. Negative Poisson's ratios in metal nanoplates. *Nat. Commun.* **2014**, *5*, 3255.
(35) Kittinger, E.; Tichý, J.; Bertagnolli, E. Example of a Negative Effective Poisson's Ratio. *Phys. Rev. Lett.* **1981**, *47*, 712−714.
(36) Evans, K. E.; Nkansah, M. A.; Hutchinson, I. J.; Rogers, S. C. Molecular network design. *Nature* **1991**, *353*, 124−124.
(37) Evans, K. E.; Alderson, A.; Christian, F. R. Auxetic two-dimensional polymer networks. An example of tailoring geometry for specific mechanical properties. *J. Chem. Soc., Faraday Trans.* **1995**, *91*, 2671−2680.
(38) Grima, J. N.; Jackson, R.; Alderson, A.; Evans, K. E. Do Zeolites Have Negative Poisson's Ratios? *Adv. Mater.* **2000**, *12*, 1912−1918.
(39) Pour, N.; Itzhaki, L.; Hoz, B.; Altus, E.; Basch, H.; Hoz, S. Auxetics at the Molecular Level: A Negative Poisson's Ratio in Molecular Rods. *Angew. Chem., Int. Ed.* **2006**, *45*, 5981−5983.
(40) Jiang, J.-W.; Kim, S. Y.; Park, H. S. Auxetic nanomaterials: Recent progress and future development. *Applied Physics Reviews* **2016**, *3*, 041101.
(41) Huang, C.; Chen, L. Negative Poisson's Ratio in Modern Functional Materials. *Adv. Mater.* **2016**, *28*, 8079−8096.
(42) Yeganeh-Haeri, A.; Weidner, D. J.; Parise, J. B. Elasticity of alpha-Cristobalite: A Silicon Dioxide with a Negative Poisson's Ratio. *Science* **1992**, *257*, 650−652.
(43) Alderson, K.; Pickles, A.; Neale, P.; Evans, K. Auxetic polyethylene: The effect of a negative poisson's ratio on hardness. *Acta Metallurgica et Materialia* **1994**, *42*, 2261−2266.
(44) LAKES, R. Foam Structures with a Negative Poisson's Ratio. *Science* **1987**, *235*, 1038−1040.
(45) Keskar, N. R.; Chelikowsky, J. R. Negative Poisson ratios in crystalline SiO2 from first-principles calculations. *Nature* **1992**, *358*, 222−224.
(46) Baughman, R. H.; Shacklette, J. M.; Zakhidov, A. A.; Stafström, S. Negative Poisson's ratios as a common feature of cubic metals. *Nature* **1998**, *392*, 362−365.
(47) Hall, L. J.; Coluci, V. R.; Galvão, D. S.; Kozlov, M. E.; Zhang, M.; Dantas, S. O.; Baughman, R. H. Sign Change of Poisson's Ratio for Carbon Nanotube Sheets. *Science* **2008**, *320*, 504−507.
(48) Mardling, P.; Alderson, A.; Jordan-Mahy, N.; Le Maitre, C. L. The use of auxetic materials in tissue engineering. *Biomater. Sci.* **2020**, *8*, 2074−2083.
(49) Park, Y. J.; Kim, J. K. The Effect of Negative Poisson's Ratio Polyurethane Scaffolds for Articular Cartilage Tissue Engineering Applications. *Advances in Materials Science and Engineering* **2013**, *2013*, 853289.
(50) Evans, K. E.; Alderson, A. Auxetic Materials: Functional Materials and Structures from Lateral Thinking. *Adv. Mater.* **2000**, *12*, 617−628.
(51) Rothenburg, L.; AI. Berlin, A.; Bathurst, R. J. Microstructure of isotropic materials with negative Poisson's ratio. *Nature* **1991**, *354*, 470−472.
(52) Gibson, L. J.; Ashby, M. F. *Cellular Solids: Structure and Properties*, 2nd ed.; Cambridge Solid State Science Series; Cambridge University Press, 1997.
(53) Milstein, F.; Huang, K. Existence of a negative Poisson ratio in fcc crystals. *Phys. Rev. B* **1979**, *19*, 2030−2033.
(54) Jiang, J.-W.; Park, H. S. Negative poisson's ratio in single-layer black phosphorus. *Nat. Commun.* **2014**, *5*, 4727.
(55) Jiang, J.-W.; Chang, T.; Guo, X.; Park, H. S. Intrinsic Negative Poisson's Ratio for Single-Layer Graphene. *Nano Lett.* **2016**, *16*, 5286−5290.
(56) He, C.; Liu, P.; Griffin, A. C. Toward Negative Poisson Ratio Polymers through Molecular Design. *Macromolecules* **1998**, *31*, 3145−3147.
(57) Baughman, R. H.; Galvão, D. S. Crystalline networks with unusual predicted mechanical and thermal properties. *Nature* **1993**, *365*, 735−737.
(58) Jin, E.; Lee, I. S.; Kim, D.; Lee, H.; Jang, W.-D.; Lah, M. S.; Min, S. K.; Choe, W. Metal-organic framework based on hinged cube tessellation as transformable mechanical metamaterial. *Science Advances* **2019**, *5*, eaav4119.
(59) Ryder, M. R.; Civalleri, B.; Cinque, G.; Tan, J.-C. Discovering connections between terahertz vibrations and elasticity underpinning the collective dynamics of the HKUST-1 metal−organic framework. *CrystEngComm* **2016**, *18*, 4303−4312.
(60) Plimpton, S. Fast parallel algorithms for short-range molecular dynamics. *J. Comput. Phys.* **1995**, *117*, 1−19.
(61) Kittel, C. *Introduction to Solid State Physics*, 6th ed.; John Wiley & Sons, Inc.: New York, 1986.
(62) Klemens, P. G. The scattering of low-frequency lattice waves by static imperfections. *Proceedings of the Physical Society. Section A* **1955**, *68*, 1113−1128.
(63) Shimizu, F.; Ogata, S.; Li, J. Theory of Shear Banding in Metallic Glasses and Molecular Dynamics Calculations. *Materials Transactions* **2007**, *48*, 2923−2927.
(64) Meza, L. R.; Das, S.; Greer, J. R. Strong, lightweight, and recoverable three-dimensional ceramic nanolattices. *Science* **2014**, *345*, 1322−1326.
(65) Giri, A.; Tomko, J.; Gaskins, J. T.; Hopkins, P. E. Large tunability in the mechanical and thermal properties of carbon nanotube-fullerene hierarchical monoliths. *Nanoscale* **2018**, *10*, 22166−22172.
(66) Talin, A. A.; Jones, R. E.; Hopkins, P. E. Metal−organic frameworks for thermoelectric energy-conversion applications. *MRS Bull.* **2016**, *41*, 877−882.
(67) Tadano, T.; Gohda, Y.; Tsuneyuki, S. Impact of Rattlers on Thermal Conductivity of a Thermoelectric Clathrate: A First-Principles Study. *Phys. Rev. Lett.* **2015**, *114*, 095501.
(68) McGaughey, A.; Kaviany, M. Thermal conductivity decomposition and analysis using molecular dynamics simulations: Part II. Complex silica structures. *Int. J. Heat Mass Transfer* **2004**, *47*, 1799−1816.
(69) Stuart, S. J.; Tutein, A. B.; Harrison, J. A. A reactive potential for hydrocarbons with intermolecular interactions. *J. Chem. Phys.* **2000**, *112*, 6472−6486.
(70) Hoover, W. G. Canonical dynamics: Equilibrium phase-space distributions. *Phys. Rev. A* **1985**, *31*, 1695−1697.

https://doi.org/10.1021/acsnano.1c09833
ACS Nano 2022, 16, 2843−2851